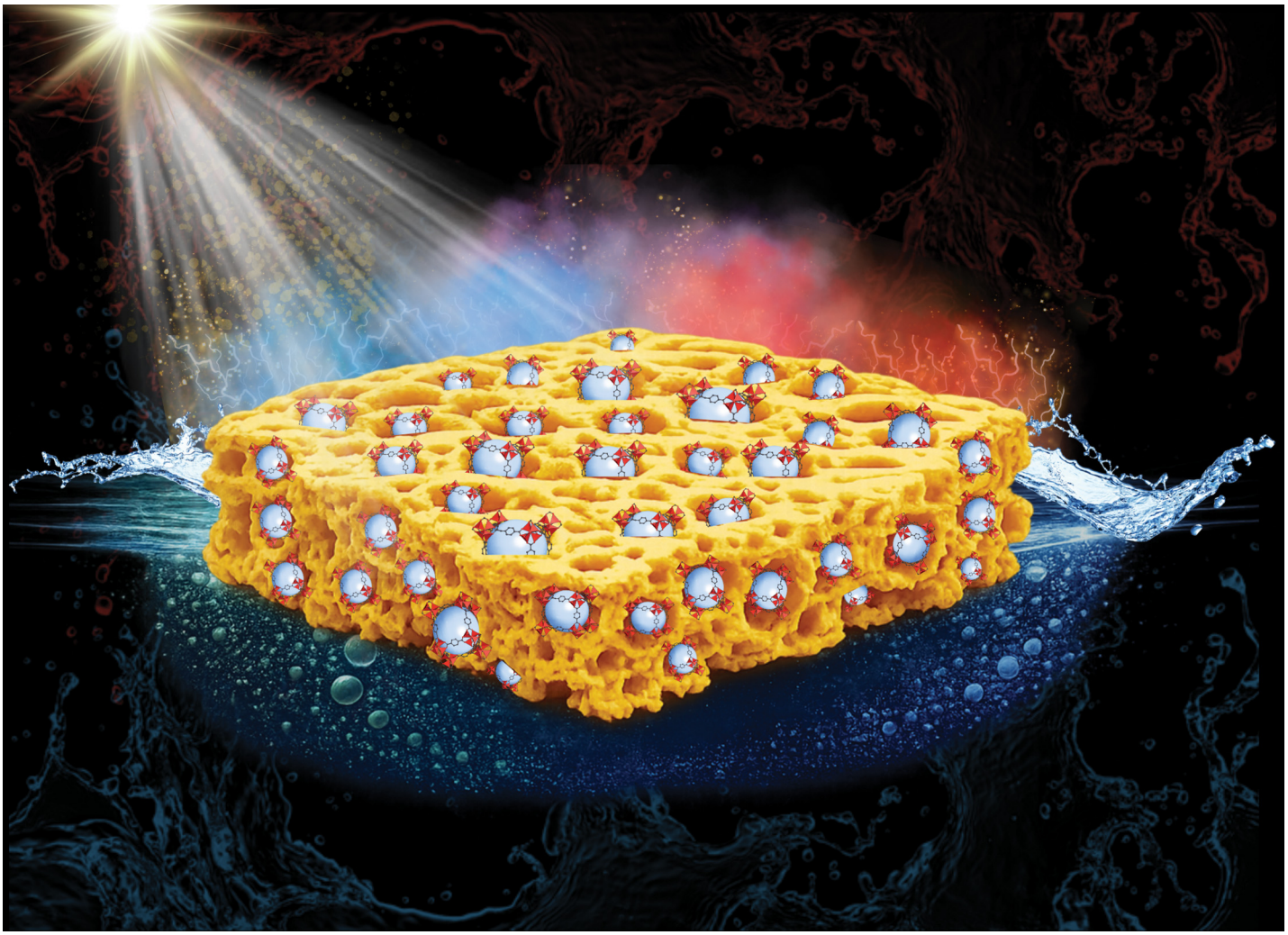

Showcasing research from Prof. Badekai Ramachandra Bhat, Catalysis and Materials Chemistry laboratory, Department of Chemistry, National Institute of Technology Karnataka, Surathkal, India.

Photo-assisted water splitting over a NiCoP/g-C_3N_4 heterostructure: understanding the role of visible light in electrochemical water splitting

A photoresponsive NiCoP/g-C_3N_4 heterostructure enables efficient electrochemical water splitting under visible-light illumination. Graphitic carbon nitride (g-C_3N_4) acts as a visible-light absorber, generating photocarriers that are effectively transferred to the catalytic sites of nickel cobalt phosphide (NiCoP). This interfacial charge-transfer synergy accelerates the kinetics of hydrogen and oxygen evolution reactions, significantly reducing overpotentials and the overall cell voltage, while delivering stable, high-efficiency water splitting at practical current densities.

Image reproduced by permission of Badekai Ramachandra Bhat from *Mater. Adv.*, 2026, **7**, 1417.

As featured in:

See Badekai Ramachandra Bhat *et al.*, *Mater. Adv.*, 2026, **7**, 1417.

ROYAL SOCIETY OF CHEMISTRY

rsc.li/materials-advances

Registered charity number: 207890

Materials Advances

ROYAL SOCIETY OF CHEMISTRY

PAPER

View Article Online
View Journal | View Issue

Cite this: *Mater. Adv.*, 2026, 7, 1417

Photo-assisted water splitting over a NiCoP/g-C_3N_4 heterostructure: understanding the role of visible light in electrochemical water splitting

Mahesha P. Nayak, [a] John D. Rodney,[bc] Sushmitha S [a] and Badekai Ramachandra Bhat *[a]

Visible-light assistance plays a pivotal role in enhancing the electrochemical reaction kinetics of photoresponsive electrocatalysts by generating additional photocarriers that participate in the interfacial HER and OER processes. Herein, we report the synthesis of a NiCo-MOF grown *in situ* on an optimised amount of g-C_3N_4 nanosheets, followed by phosphidation to yield a NiCoP/g-C_3N_4 heterostructure *via* a two-step process. The electrocatalytic performance of the NiCoP/g-C_3N_4 heterostructure was systematically evaluated under both visible-light irradiation and in the dark. Under visible-light illumination, the catalyst required overpotentials of 222 mV and 210 mV (*iR*-corrected) for HER and OER, respectively, at a current density of 100 mA cm^{-2} with Tafel slopes of 85.9 mV dec^{-1} and 68.8 mV dec^{-1}. In contrast, under dark conditions, the overpotentials increased to 277 mV and 260 mV (*iR*-corrected) for the HER and OER, with Tafel slopes of 98.8 mV dec^{-1} and 86.5 mV dec^{-1}, respectively. Notably, the overpotentials required are reduced by 1.25 times compared to dark conditions. Furthermore, in a two-electrode system comprising NiCoP/g-C_3N_4‖NiCoP/g-C_3N_4, a cell voltage of 1.57 V under illumination and 1.65 V in the dark was required to achieve a current density of 10 mA cm^{-2}. The catalyst also demonstrated excellent stability, maintaining activity for 24 hours at a high current density of 400 mA cm^{-2} without noticeable degradation, and delivering a faradaic efficiencies of 97% for HER and 96% for OER under illumination. This study highlights how visible-light integration, *via* photoexcitation of g-C_3N_4 and synergistic coupling with NiCoP, enhances electrochemical water splitting performance, providing a practical strategy for designing highly efficient heterointerface electrocatalysts for photo-assisted water splitting.

Received 4th November 2025,
Accepted 13th January 2026

DOI: 10.1039/d5ma01279a

rsc.li/materials-advances

1. Introduction

Hydrogen, with its high energy density (142 MJ kg^{-1}) and clean combustion characteristics, is considered a promising solution for a sustainable and efficient energy carrier system.[1,2] Among the various production methods, electrocatalytic water splitting is particularly attractive due to its high efficiency and increasing industrial maturity.[3] This process involves two fundamental half-cell reactions: the hydrogen evolution reaction (HER) and the oxygen evolution reaction (OER). Thermodynamically, a Gibbs free energy change (ΔG) of 237.2 kJ mol^{-1} is required to drive overall water splitting, corresponding to a reversible cell potential (ΔE) of 1.23 V. However, the major challenge lies in the development of cost-effective electrocatalysts that not only rival the activity of commercial noble-metal-based catalysts but also efficiently overcome the sluggish kinetics of both HER and OER.[4]

Metal–organic frameworks (MOFs), particularly bimetallic systems, have attracted considerable attention as promising candidates for application in electrocatalysis,[5,6] supercapacitors,[7] gas storage, and separation.[8,9] Their advantages arise from the high surface area, tunable electronic structures, abundant active sites, rich redox chemistry, and low cost, which collectively promote efficient charge transfer and mass transport throughout the electrochemical process.[10] Notably, the synergistic interplay between different redox-active metal centres in bimetallic MOFs markedly enhances catalytic activity compared to their monometallic counterparts.[11] To further enhance the catalytic performance of pristine MOF-based systems, recent efforts have focused on incorporating semiconducting components or

[a] *Department of Chemistry, Catalysis, and Materials Chemistry Laboratory, National Institute of Technology Karnataka, Surathkal, D.K., Karnataka 575 025, India. E-mail: ram@nitk.edu.in*
[b] *Department of Physics, Saveetha School of Engineering, Saveetha Institute of Medical and Technical Sciences, Chennai 602105, India*
[c] *Department of Advanced Components and Materials Engineering, Sunchon National University, 255, Jungang-ro, Suncheon-si, Jeollanam-do 57922, Republic of Korea*

heteroatoms into the MOF architecture,[12,13] where Ubaidullah *et al.* reported a ZnO@NMC nanocomposite derived from MOF-5, which served as an efficient hybrid bifunctional electrocatalyst, delivering overpotentials of 0.39 V for the HER and 0.57 V for the OER at 10 mA cm^{-2}.[14] Similarly, Shabbir B *et al.* synthesised Pr-MOF/Fe_2O_3 *via* a hydrothermal route, which exhibited an OER overpotential of 238 mV at a current density of 10 mA cm^{-2} and a low Tafel slope of 37 mV dec^{-1}.[15] Khan S *et al.* used the hydrothermal method to synthesise g-C_3N_4@ZIF-67 composites with varying g-C_3N_4 loadings (1–8 wt%). The 3 wt% g-C_3N_4@ZIF-67 composite exhibited excellent bifunctional activity for the HER and OER with low overpotentials of 152 mV and 176 mV at 10 mA cm^{-2} in alkaline media and achieved overall water splitting at 1.34 V and remained stable for 24 h. The enhanced performance was attributed to improved charge transfer, a high surface area, and the hydrophilic nature of the optimised material (contact angle 54.4°).[16] This strategy has shown considerable promise in advancing both electrochemical and photoelectrochemical water-splitting applications.[17] In particular, when MOFs are modified to incorporate photoactive components, it becomes crucial to account for the influence of visible light during electrocatalytic evaluation. The introduction of a photoactive component can lead to significant variations in catalytic activity under illuminated and dark conditions, which is a key component that plays a critical role in the overall performance.[18] In the context of electrochemical water splitting, coupling a photoactive semiconductor with an electrocatalyst enables photo-assisted electrocatalysis, where visible light-generated charge carriers directly contribute to the electrochemical half-reactions.

Among several photoactive components, graphitic carbon nitride (g-C_3N_4), an organic semiconductor, has garnered significant attention in recent years for photocatalytic applications. It has unique properties, such as exceptional chemical and thermal stability,[19] abundant active sites, an optimal band gap (~2.7 eV) for visible-light absorption, and a favourable valence band position (−0.93 V *vs.* NHE at pH = 0) for driving both water oxidation and reduction, making it a highly promising photocatalyst.[20–22] g-C_3N_4 also has the ability to form composites with inorganic materials and MOFs, which will arise from the interaction of unpaired π-electrons and surface oxy, hydroxy and amine functional groups.[23] In addition, the facile synthesis, two-dimensional layered structure, and low cost of g-C_3N_4 further validate its enhanced appeal as a sustainable material for photocatalysis. However, despite all of these advantages, g-C_3N_4 suffers from intrinsic limitations, such as its low surface area and rapid recombination of photogenerated charge carriers, which significantly hinder its efficiency.[24] To overcome these challenges and promote effective charge separation, incorporating co-catalysts, constructing heterojunctions with other semiconductors, and introducing metal or non-metal dopants into its layered framework are commonly employed strategies.

In this study, a NiCoP/g-C_3N_4 heterostructure was synthesised *via in situ* growth of NiCo-2-methylimidazole on an optimised amount of g-C_3N_4, followed by a phosphidation process. By systematically comparing the catalytic performance of NiCoP/g-C_3N_4 under dark and visible-light-illuminated conditions, this work dissects the specific contribution of visible light to the overall water-splitting reaction, demonstrating how photoexcitation of g-C_3N_4 lowers the operational overpotential and enhances the reaction kinetics in a practical electrochemical configuration. The engineered NiCoP/g-C_3N_4 interface provides abundant accessible active sites and facilitates efficient charge-transport pathways, thereby improving the bifunctional electrocatalytic performance toward both HER and OER in alkaline media. Under visible-light illumination, notable enhancements in overpotential, faradaic efficiency and reaction kinetics are observed relative to dark operation, while the catalyst also exhibits outstanding durability in both two and three-electrode configurations, maintaining stable operation for 24 hours at high current densities. These findings underscore the potential of the NiCoP/g-C_3N_4 heterostructure as a robust and efficient bifunctional electrocatalyst for visible-light assisted overall water splitting.

2. Experimental methods

2.1. Synthesis of g-C_3N_4 and NiCoP/g-C_3N_4

2.1.1. Preparation of g-C_3N_4. g-C_3N_4 was prepared *via* thermal polymerisation of melamine. 5 g of melamine was placed in a covered silica crucible and heated in a muffle furnace at 550 °C for 4 hours at a ramp rate of 5 °C min^{-1}. After natural cooling to room temperature, the pale-yellow powder was washed several times with deionised water to remove residual impurities, then dried in a vacuum oven at 80 °C for 12 h. The schematic representation of the synthesis is shown in Fig. 1(a).

2.1.2. *In situ* growth of NiCo-MOF on g-C_3N_4. 2-Methylimidazole (8 mmol) was dissolved in 25 mL of methanol under constant magnetic stirring. To this, predetermined amounts of g-C_3N_4 were introduced to prepare NiCo-MOF/*x*-wt% g-C_3N_4 (*x* = 2.5, 5.0, and 7.5 wt%) composites, followed by 30 min of stirring to ensure homogeneous dispersion. Separately, cobalt(II) nitrate hexahydrate (2 mmol) and nickel(II) nitrate hexahydrate (2 mmol) were dissolved in 25 mL of methanol and stirred for 15 min to obtain a clear precursor solution. This metal salt solution was then added dropwise to the 2-methylimidazole/g-C_3N_4 dispersion under continuous stirring. The resulting purple suspension was treated with ultrasonication (100 W) for 30 min, followed by an additional 30 min of magnetic stirring. The mixture was subsequently heated at 70 °C under reflux conditions for 12 h. The final product was recovered by centrifugation, washed three times with methanol, and dried at 60 °C for 8 h. The pristine NiCo 2-methylimidazole-MOF was synthesised under identical conditions without adding g-C_3N_4 and designated as NiCo-MOF.

2.1.3. Synthesis of NiCoP/g-C_3N_4. Based on electrochemical optimisation studies, the NiCo-MOF containing 5 wt% g-C_3N_4 exhibited good catalytic activity for both HER and OER. Therefore, the subsequent phosphidation was performed using the NiCo-MOF/5 wt% g-C_3N_4 sample. The optimised NiCo-MOF/5 wt% g-C_3N_4 precursor (40 mg) and sodium hypophosphite

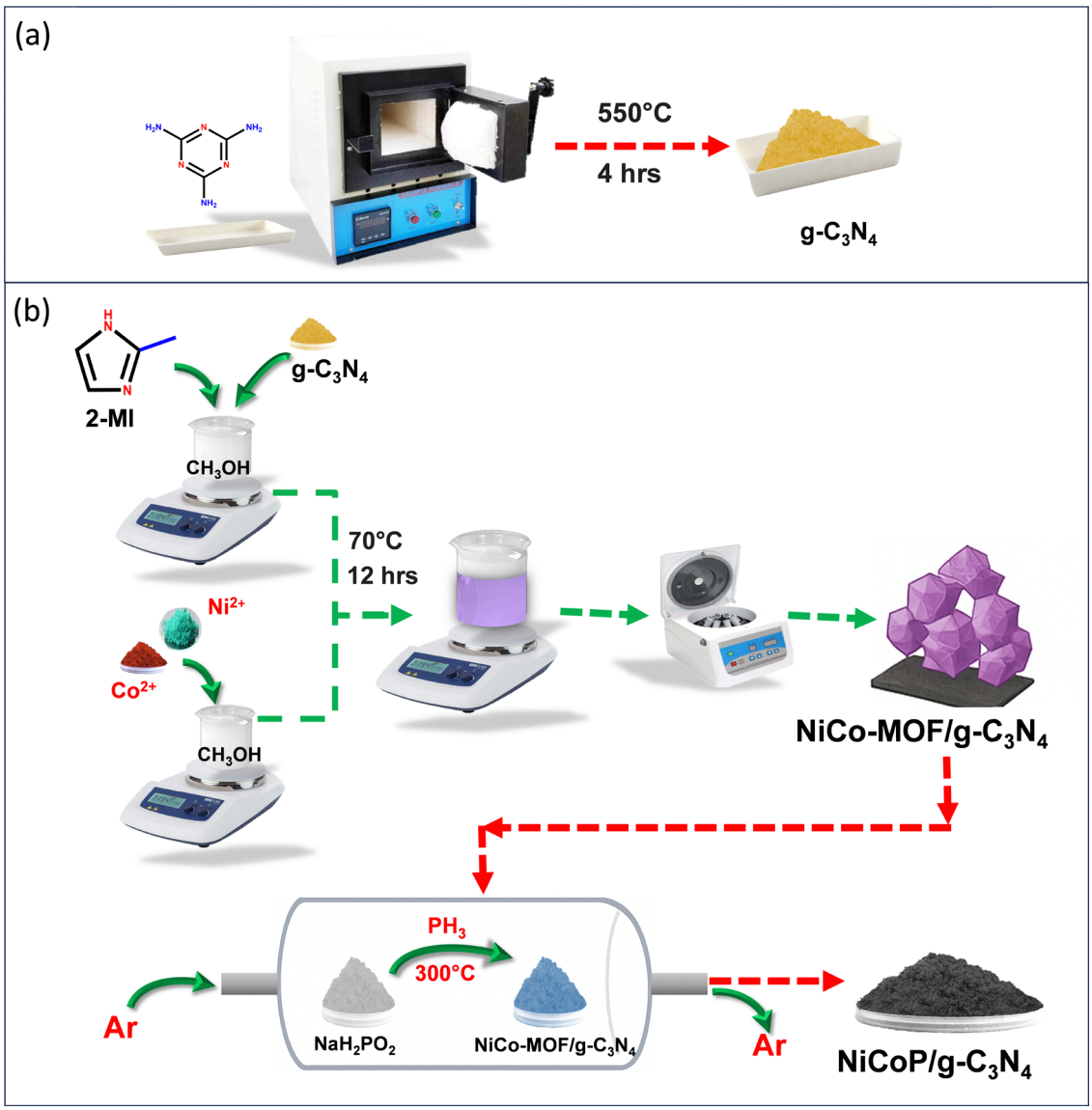

Fig. 1 Schematic representation of the synthesis of (a) g-C_3N_4, and (b) NiCoP/g-C_3N_4.

monohydrate (120 mg) were placed in separate alumina boats, with $NaH_2PO_2{\cdot}H_2O$ positioned at the upstream side of a tubular furnace.[25] The system was heated to 300 °C at a rate of 10 °C min^{-1} and the temperature was maintained for 2 h under a continuous argon flow. During heating, $NaH_2PO_2{\cdot}H_2O$ decomposed to release PH_3, which promoted the phosphidation of Ni and Co species in the composite, leading to the formation of bimetallic phosphides. The resulting product was thoroughly washed with deionised water and ethanol, followed by drying in a vacuum oven at 60 °C for 12 h. The schematic illustration of the synthesis of NiCo-MOF/*x*-wt% g-C_3N_4 and NiCoP/g-C_3N_4 is shown in Fig. 1(b).

3. Material characterisation

The XRD patterns of g-C_3N_4 and NiCoP/g-C_3N_4 are presented in Fig. 2(a). Distinct diffraction peaks for g-C_3N_4 appear at 12.9° and 27.7°, which can be indexed to the (100) and (002) planes, respectively. The reflection at 12.9° is associated with the in-plane structural ordering of triazine units, whereas the peak at 27.7° corresponds to the interlayer stacking of the conjugated aromatic frameworks along the (002) direction.[26] After phosphidation, the XRD profile of the NiCoP/g-C_3N_4 composite exhibited distinct diffraction peaks ascribed to NiCoP, alongside the characteristic reflections of g-C_3N_4. These peaks were consistent with those of pristine NiCoP and matched well with the standard reference card (PDF#71-2336). The diffraction maxima observed at 40.8°, 44.6°, 48.3°, and 56.1° were indexed to the (111), (201), (210), and (211) crystallographic planes of NiCoP, respectively.[27] The composite retains the representative diffraction features of both g-C_3N_4 and NiCoP, suggesting that the intrinsic crystalline frameworks of the two components were preserved within the heterostructure. The average crystallite size of the composite was determined using the Debye–Scherrer equation, and was estimated to be ~14.25 nm.

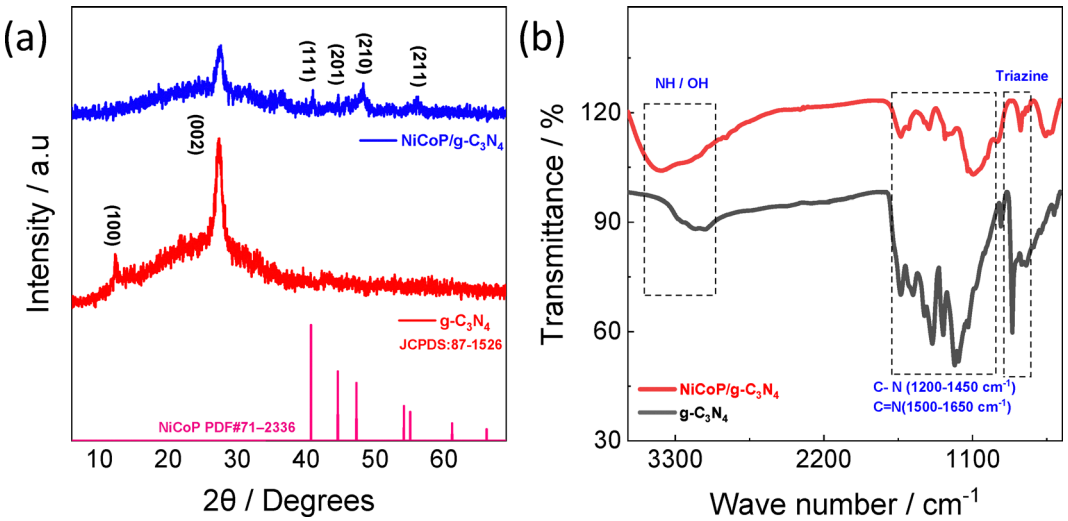

Fig. 2 (a) XRD analysis of g-C_3N_4 and NiCoP/g-C_3N_4 and (b) FTIR analysis of g-C_3N_4 and NiCoP/g-C_3N_4.

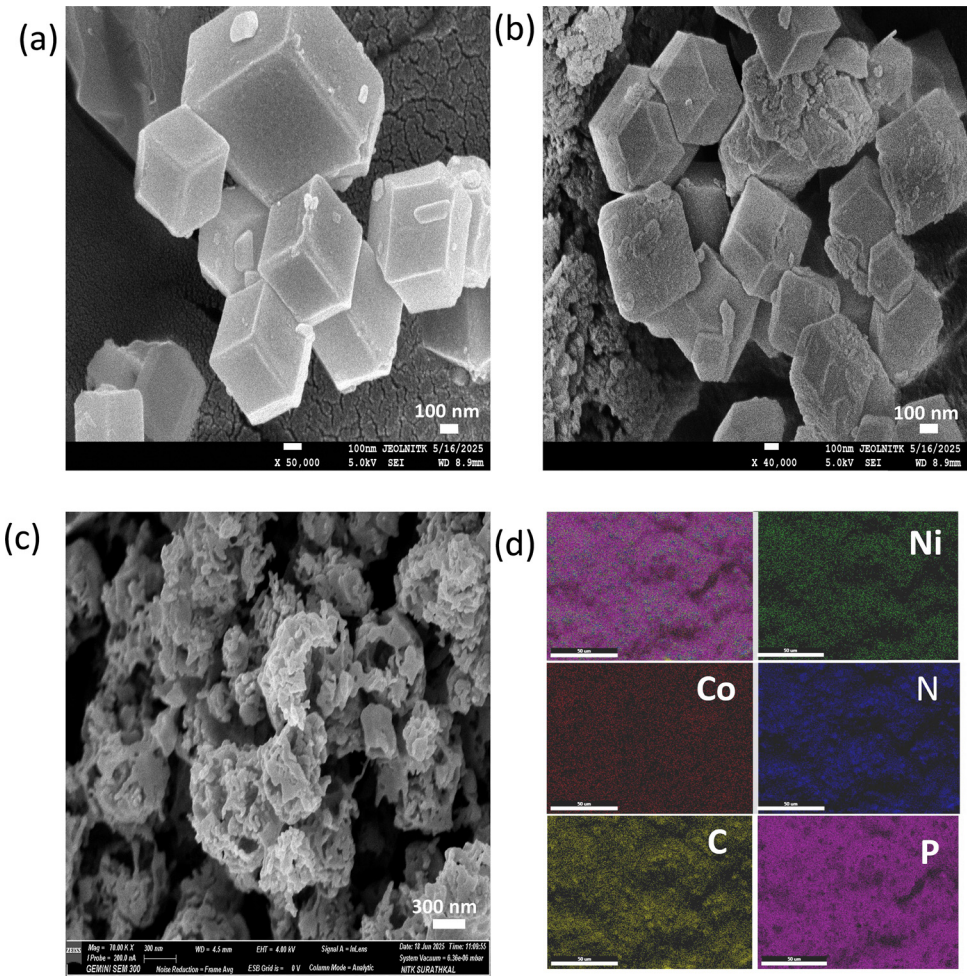

Fig. 3 FESEM of (a) NiCo-MOF, (b) NiCo-MOF/g-C_3N_4, (c) NiCoP/g-C_3N_4, and (d) colour mapping of NiCoP/g-C_3N_4, and corresponding elemental mapping (Ni, Co, N, C, P).

FT-IR spectroscopy was employed to investigate the surface chemistry of the NiCoP/g-C_3N_4 nanocomposites. As depicted in Fig. 2(b), characteristic absorption features were observed for both pristine g-C_3N_4 and the NiCoP/g-C_3N_4 composite within the 500–2500 cm^{-1} region. The band at 803 cm^{-1} is assigned to the breathing vibration of the tri-*s*-triazine units, while multiple absorptions in the 1200–1600 cm^{-1} range correspond to the stretching vibrations of C–N linkages in g-C_3N_4. Additional peaks at 1380 cm^{-1} and 1577 cm^{-1} can be attributed to COO^- stretching, indicating the successful carboxylation of the composite surface.[28,29] A broad absorption band between 3000 cm^{-1} and 3500 cm^{-1} is attributed to –NH stretching from terminal $-NH_2$ groups and –OH groups from adsorbed water, suggesting incomplete condensation of amino functionalities.[27] The incorporation of NiCoP did not significantly modify the characteristic features of g-C_3N_4, confirming the preservation of its intrinsic microstructure in the composite.

The morphological transformation of the NiCo-MOF, NiCo-MOF/g-C_3N_4, and NiCoP/g-C_3N_4 was characterised by FESEM analysis, as illustrated in Fig. 3(a)–(c), respectively. Pristine NiCo-MOF (Fig. 3(a)) exhibits uniform cubic microcrystals with smooth faces indicative of high crystallinity and a well-defined MOF architecture. Fig. 3(b) depicts the structure of NiCo MOF/g-C_3N_4, where the structural framework remains largely intact, with a slight increase in surface roughness, indicating the growth of g-C_3N_4 layers on the MOF architecture, which facilitates the contact between the MOF and g-C_3N_4 nanosheets. Fig. 3(c) depicts the porous cubic networks composed of sponge-like nanoclusters formed in the NiCoP/g-C_3N_4 composite after phosphidation. This porous morphology is expected to facilitate electrolyte penetration and maximise the exposure of active catalytic sites. Elemental mapping presented in Fig. 3(d) confirms the homogeneous distribution of Ni, Co, P, C, and N throughout the NiCoP/g-C_3N_4 matrix. The EDS map in Fig. S4 reveals the distribution of all elements within the material, further confirming the composition of the NiCoP/g-C_3N_4.

The TEM and HRTEM images of the NiCoP/g-C_3N_4 nanocomposite are presented in Fig. 4. g-C_3N_4 displays a typical two-dimensional nanosheet morphology, while darker NiCoP nanoparticles are uniformly distributed over the nanosheet surface, as shown in Fig. 4a and b, confirming the successful formation of the NiCoP/g-C_3N_4 composite. The homogeneous dispersion of NiCoP nanoparticles on the g-C_3N_4 surface suggests strong interfacial interaction between the two components, which is

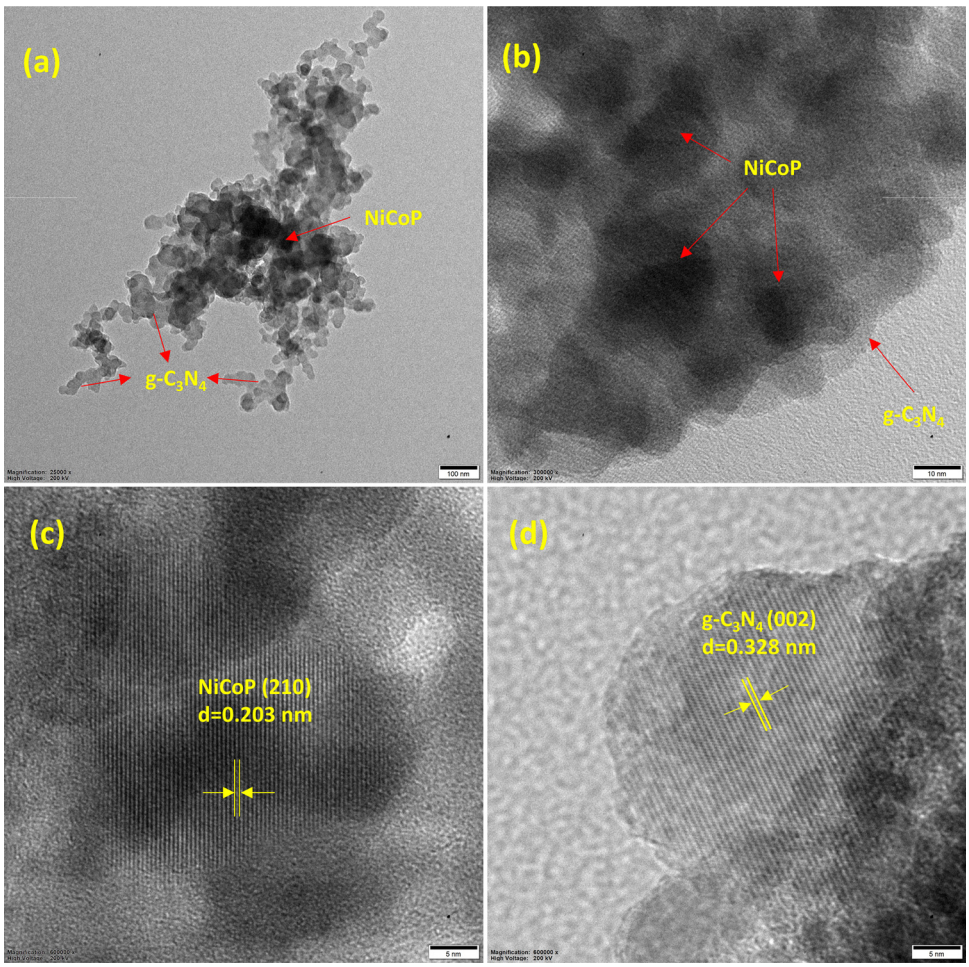

Fig. 4 (a) and (b) TEM images of NiCoP/g-C_3N_4, and (c) and (d) HR TEM images of NiCoP/g-C_3N_4.

favourable for efficient charge transfer. The HR-TEM image in Fig. 4c shows clear lattice fringes with an interplanar spacing of about 0.203 nm, indexed to the (210) plane of NiCoP, confirming the crystalline nature of the phosphide phase. The lattice spacing of 0.328 nm, as observed in Fig. 4d, corresponds to the (002) plane, which is consistent with the XRD results of g-C_3N_4.

The comprehensive elemental composition and surface chemical states of the NiCoP/g-C_3N_4 material were analysed using XPS. The survey spectrum, as shown in Fig. 5(a), confirmed the presence of Ni 2p, Co 2p, P 2p, C 1s, N 1s, and O 1s signals, verifying the successful incorporation of all expected elements. Gaussian fitting was employed to deconvolute the spectra.

The deconvoluted Ni 2p spectrum presented in Fig. 5(b) shows peaks at 851.8 eV and 860.4 eV, corresponding to Ni $2p_{3/2}$ and its satellite peak, while the peaks at 868.1 eV and 880.9 eV correspond to Ni $2p_{1/2}$ and its satellite peak, respectively, which are assigned to nickel in the Ni–P bond, confirming that the phosphidation process induced partial covalent bonding between Ni and P.[30,31] A peak at 872.6 eV is assigned to a Ni oxide species, suggesting the presence of surface oxidised Ni species.[32,33] The deconvoluted Co 2p spectrum shown in Fig. 5(c) displays distinct features corresponding to the Co $2p_{3/2}$ and Co $2p_{1/2}$ spin–orbit components. Peaks located at 776.1 and 793.6 eV are assigned to the Co–P bond, confirming the successful formation of cobalt phosphide.[34,35] The major peaks observed at 783.7 eV (Co $2p_{3/2}$) and 799.6 eV (Co $2p_{1/2}$) are attributed to Co^{2+} species ($CoO/Co(OH)_2$), arising from surface oxidation of the samples.[36,37] In addition, satellite features are evident at 789.2 eV and 805.9 eV, corresponding to the Co $2p_{3/2}$ and Co $2p_{1/2}$ states, respectively. The N 1s spectrum shows peaks at 399.3 eV and 400.8 eV as shown in Fig. 5(d), corresponding to sp^3-hybridised nitrogen (N–$(C)_3$) and C=N functionalities within aromatic CN heterocycles, respectively.[38] An additional peak at 402.2 eV is assigned to nitrogen atoms associated with amino functional groups.[39] The high-resolution C 1s spectrum in Fig. 5(e) reveals two prominent peaks at 285.5 eV and 288.5 eV. The peak at 285.5 eV is attributed to adventitious carbon associated with sp^3-hybridised C–C bonding, while the peak at 288.5 eV corresponds to C=N bonding environments.[38] The P 2p spectrum of Fig. 5(f) exhibits a small and broad peak at 129.9 eV, assigned to the P $2p_{3/2}$ component, indicating the formation of Ni/Co–P bonds in the NiCoP/g-C_3N_4 catalyst.[40] Additional peaks at 133.7 eV and 136.2 eV correspond to oxidised phosphorus species (P $2p_{3/2}$), attributed to the surface oxidation of the phosphide phase.[41–43] Moreover, compared with the standard XPS data reported for pure g-C_3N_4, the C 1s and N 1s peaks of NiCoP/g-C_3N_4 exhibit slight binding-energy shifts. Such core-level shifts of C 1s/N 1s in g-C_3N_4 based heterostructures, together with the appearance of metal-phosphide features, are interpreted as indirect evidence of interfacial electronic interaction and charge redistribution between the metal phosphide phase and the g-C_3N_4 framework.[2,44]

According to the Kubelka–Munk function, the Tauc plots of g-C_3N_4, NiCoP, and NiCoP/g-C_3N_4 are presented in Fig. 6(a), yielding band gaps (E_g) of 2.7 eV, 1.4 eV, and 2.1 eV, respectively. The notable reduction in the bandgap of the composite is attributed to interfacial electronic coupling at the heterojunction, which introduces additional states near the valence band edge. These interfacial states facilitate bandgap narrowing, extending optical absorption into the visible region and

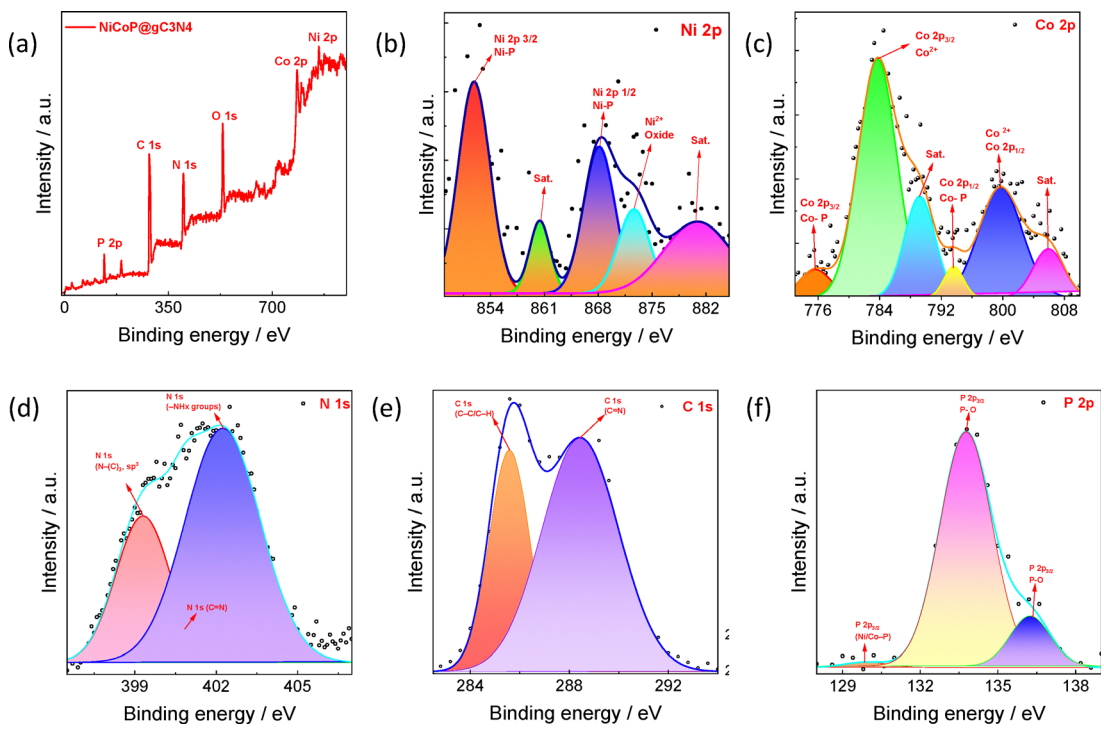

Fig. 5 XPS spectra of NiCoP/g-C_3N_4: (a) survey spectra of NiCoP/g-C_3N_4, (b) Ni 2p, (c) Co 2p, (d) N 1s, (e) C 1s, and (f) P 2p.

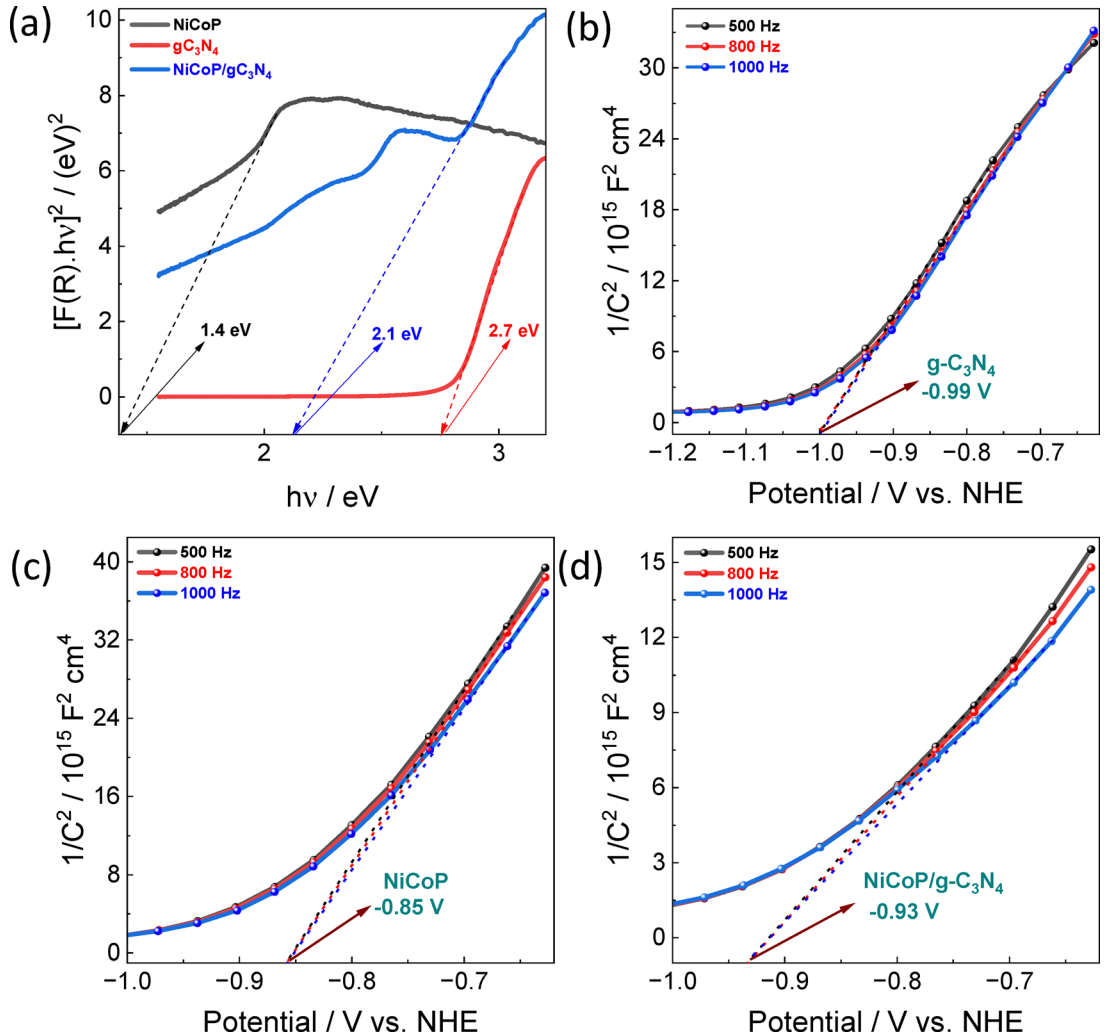

Fig. 6 (a) Tauc plots of g-C_3N_4, NiCoP, and NiCoP/g-C_3N_4; (b)–(d) are Mott–Schottky plots of g-C_3N_4, NiCoP, and NiCoP/g-C_3N_4, respectively.

enhancing photocatalytic activity.[27,45] Fig. 6(b)–(d) shows the Mott–Schottky (M–S) plots of g-C_3N_4, NiCoP, and NiCoP/g-C_3N_4, respectively, recorded at different frequencies (500 Hz, 800 Hz, and 1000 Hz). All samples exhibit positive slopes, confirming their n-type semiconducting behaviour. The flat-band potentials (E_{fb}), determined from the *x*-axis intercepts, are −0.99, −0.85, and −0.93 V *vs.* Ag/AgCl (sat. KCl), for the g-C_3N_4, NiCoP and NiCoP/g-C_3N_4 composite, respectively. The slight increase in E_{fb} for NiCoP/g-C_3N_4 relative to g-C_3N_4, and its slight decrease relative to NiCoP, indicates interfacial electron redistribution within the composite.

$$E_{CB}\ (vs.\ \text{NHE}) = E_{fb}\ (vs.\ \text{Ag/AgCl}) + 0.198 - 0.0591 \times \text{pH} \quad (1)$$

$$E_{VB} = E_{CB} + E_g \quad (2)$$

According to eqn (1), the conduction band potential (E_{CB}) values of g-C_3N_4, NiCoP, and NiCoP/g-C_3N_4 were estimated to be −1.62 V, −1.48 V, and −1.56 V *vs.* NHE, with corresponding valence band potential (E_{VB}) values of +1.08 V, −0.08 V, and +0.54 V *vs.* NHE, calculated from eqn (2). These findings suggest that the band edges of NiCoP/g-C_3N_4 are positioned between those of g-C_3N_4 and NiCoP, confirming that its band gap lies intermediate to the two parent materials.

A plausible reaction mechanism for the NiCoP/g-C_3N_4 system is illustrated in Fig. 7. Under visible-light irradiation, the moderate band gap of g-C_3N_4 (2.7 eV) enables the excitation of electrons from the valence band (VB) to the conduction band (CB), resulting in the generation of electron–hole pairs. The E_{CB} of g-C_3N_4 (−1.62 V *vs.* NHE) is more negative than that of NiCoP (−1.48 V *vs.* NHE), facilitating downhill electron transfer from g-C_3N_4 to NiCoP. The transferred electrons are subsequently directed to the Ni foam substrate, where, assisted by the applied bias, they efficiently participate in proton reduction at the cathode to generate H_2.

Meanwhile, the VB potential of g-C_3N_4 (+1.08 V *vs.* NHE) is more positive, indicating that the photogenerated holes possess sufficient oxidising power to drive the OER. These holes on the g-C_3N_4 surface migrate toward the electrode/electrolyte interface, where they oxidise surface-adsorbed H_2O/OH^- species.[46] In parallel, NiCoP undergoes surface reconstruction under anodic conditions to form Ni/Co oxyhydroxide species,

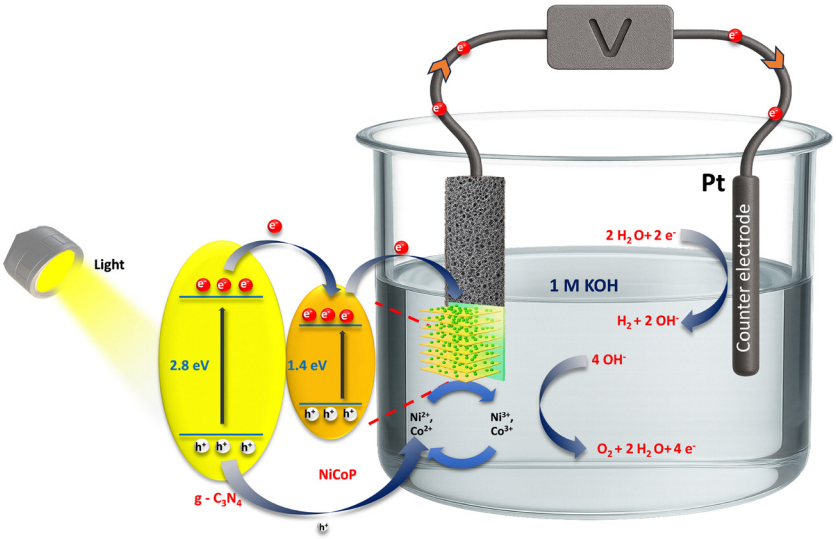

Fig. 7 Proposed mechanism for the HER and OER under visible light illumination.

and the photogenerated holes (together with the applied bias) further oxidise Ni^{2+}/Co^{2+} to high-valence Ni^{3+}/Co^{3+} states, which serve as catalytically active centres for O_2 evolution. The oxidised Ni/Co oxyhydroxides mediate the conversion of surface-bound H_2O/OH^- into O_2 *via* oxyhydroxide intermediates. After O_2 release, the high-valence Ni/Co species are reduced back to Ni^{2+}/Co^{2+}, thereby completing and sustaining the catalytic cycle.[47]

The visible light response of the composites was investigated through CV analysis in a 3-electrode configuration with 1 M KOH electrolyte, as shown in Fig. 8(a). Notably, the anodic and cathodic currents of NiCoP/g-C_3N_4 under illumination were comparatively higher than those recorded under dark conditions. The number of electrons participating in the redox process was estimated from the reduction peaks observed in the CV curves, as shown in Fig. S1(a) and (b), following the procedure outlined in ref. 48, the calculated electron transfer values were 3.95×10^{21} and 4.92×10^{21} for dark and illuminated conditions, respectively. The enhanced electron transfer can be ascribed to the increased photogenerated charge carriers and their effective separation at the heterostructure interface. This highlights the critical role of light in enhancing charge dynamics by increasing the accessible active surface area, accelerating electron transport, and thereby promoting stronger synergistic interactions at the NiCoP/g-C_3N_4 heterojunction.[18,49]

EIS was performed to investigate the charge-transfer behaviour of NiCoP/g-C_3N_4 under dark and illuminated conditions. As shown in the Nyquist plots in Fig. 8(b), the illuminated NiCoP/g-C_3N_4 electrode illustrates the smallest semicircular arc in the high-frequency region compared to under dark conditions, signifying a markedly reduced charge-transfer resistance (R_{ct}).[50] The impedance spectra were fitted to an $R(C(R(QR)))(CR)$ equivalent circuit, which comprises the solution resistance (R_S), charge-transfer resistance (R_{ct}), double-layer capacitance (C_{dl}), and constant-phase elements. The various circuit parameters are summarised in Table S1. In the presence of visible light, the NiCoP/g-C_3N_4 electrode exhibits improved conductivity, with $R_S = 1.00\ \Omega$, $C_{dl} = 45.7$ mF, and $R_{ct} = 0.373\ \Omega$, indicating efficient interfacial charge transport. Upon illumination, g-C_3N_4 efficiently generates electron–hole pairs, and the photogenerated electrons are rapidly separated across the heterointerface, leading to an increased surface charge density. These electrons are subsequently transferred to the conductive NiCoP framework,

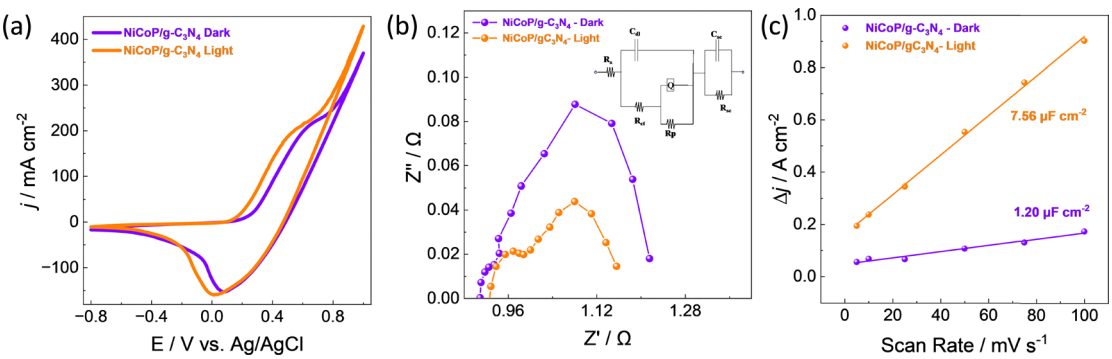

Fig. 8 (a) CV of NiCoP/g-C_3N_4 in the dark and illuminated conditions, (b) Nyquist plot of NiCoP/g-C_3N_4 in the dark and illuminated conditions fitted with $R(C(R(QR)))(CR)$ circuit, and (c) electrochemical double-layer capacitance (C_{dl}) of the NiCoP/g-C_3N_4 in the dark and illuminated conditions.

where they participate in redox processes. The synergistic interaction between the photoexcited electrons from g-C_3N_4 and the redox-active Ni and Co centres facilitates accelerated interfacial charge transfer, thereby improving the overall electrocatalytic activity under illuminated conditions.

The double-layer capacitance ($2C_{dl}$) values of the NiCoP/g-C_3N_4 were measured in dark and illuminated conditions, as shown in Fig. 8(c). The capacitance was measured to be 1.20 μF cm^{-2} in the dark and 7.56 μF cm^{-2} under illumination, with corresponding measured ECSA values of 0.015 cm^2 and 0.0945 cm^2, respectively. The substantial increase in ECSA under visible-light exposure underscores the crucial role of g-C_3N_4 incorporation in enhancing surface activity. This improvement arises from more favourable charge-carrier dynamics under illumination, where the generation of photoinduced electron–hole pairs activates additional electroactive sites, thereby increasing surface accessibility and reactivity.[51] The substantial rise in double-layer capacitance further confirms the photo-responsive character of the catalyst.

The CV was measured for the NiCoP/g-C_3N_4 electrode under both dark and light conditions, at scan rates ranging from 5 to 100 mV s^{-1} as shown in Fig. S1(c) and (d). The g-C_3N_4 plays a crucial role under visible-light irradiation by generating additional photogenerated charge carriers, so under illuminated conditions, an apparent increase in both anodic and cathodic current densities was observed with increasing scan rates, reflecting the rapid and reversible redox transitions of the Ni and Co centres and efficient charge-transfer dynamics.[52,53]

Fig. 9(a) presents the *iR*-corrected LSV polarisation curves of the NiCoP/g-C_3N_4 electrode, recorded under both dark and illuminated conditions using a three-electrode setup at a scan rate of 5 mV s^{-1} to evaluate its light-assisted electrocatalytic HER performance. Under illumination, the NiCoP/g-C_3N_4 electrode exhibits a significantly reduced overpotential of 222 mV at a current density of 100 mA cm^{-2}, compared to 277 mV under dark conditions. Furthermore, under illuminated conditions, the catalyst exhibited a TOF of 6.35 × 10^{-5} s^{-1}. This

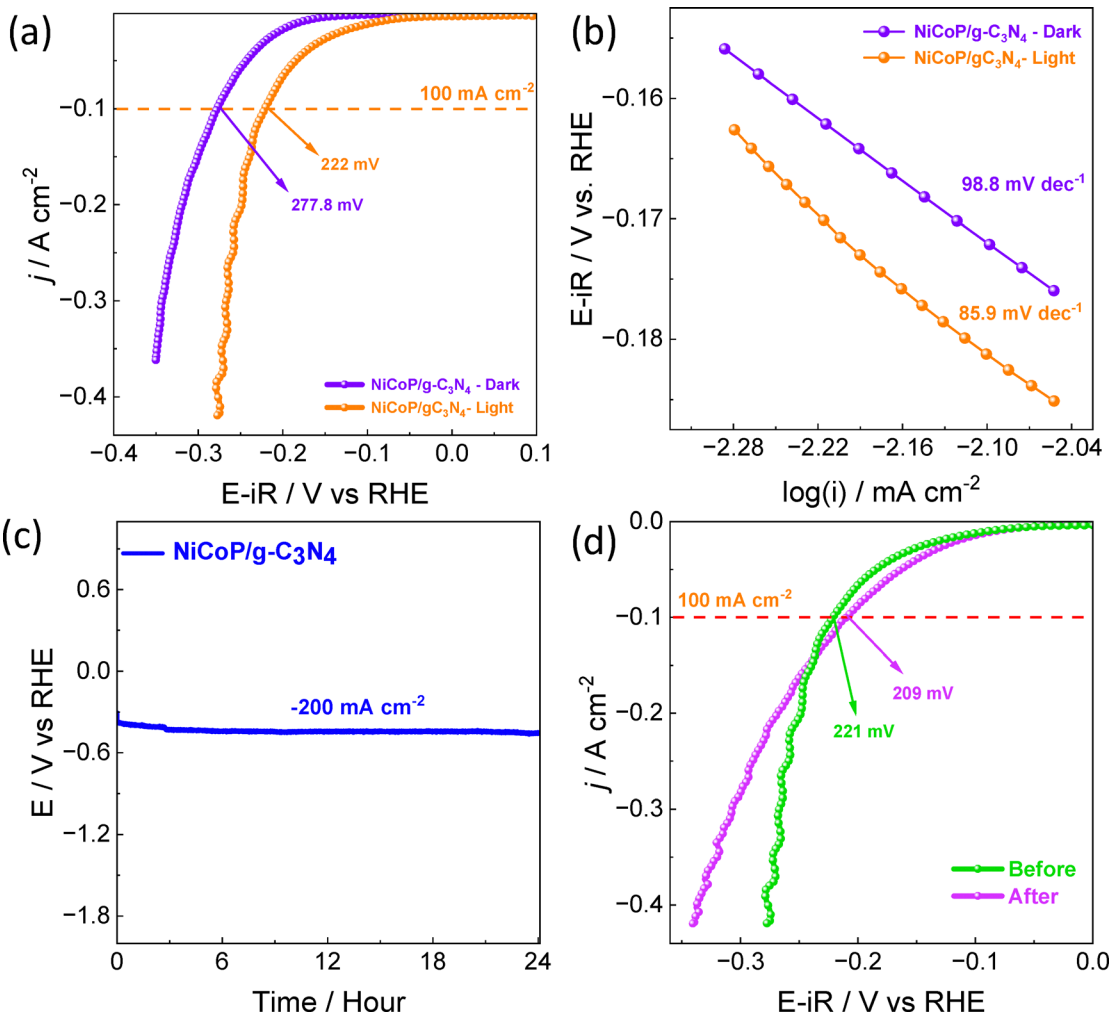

Fig. 9 (a) *iR* corrected LSV of NiCoP/g-C_3N_4 in dark and illuminated conditions, (b) Tafel plot of NiCoP/g-C_3N_4 in dark and illuminated conditions, (c) 24 hours of chronopotentiometry test for NiCoP/g-C_3N_4 under illuminated conditions at a current density of −200 mA cm^{-2}, and (d) *iR* corrected LSV of NiCoP/g-C_3N_4 in illuminated conditions before and after the chronopotentiometry test.

enhanced HER activity is attributed to the synergistic effects of the optimised integration of g-C_3N_4, favourable metal–ligand coordination, and the presence of redox-active Ni and Co centres, and also that the enhanced photoinduced catalytic activity arises from heterojunction-induced charge separation, which suppresses recombination and boosts catalytic efficiency[54] collectively delivering a performance approximately 1.25 times higher than that observed in under dark conditions.

The Tafel slopes of the synthesised electrocatalysts are presented in Fig. 9(b). Notably, the NiCoP/g-C_3N_4 catalyst under light illumination exhibits a significantly lower Tafel slope of 85.9 mV dec^{-1} compared to 98.8 mV dec^{-1} under dark conditions. Upon illumination, the photo-generated electrons move towards the surface of NiCoP through the heterointerface, thereby enhancing the surface charge density and facilitating water dissociation and hydrogen adsorption on the surface, which accelerates the Volmer step.[55] Consequently, the rate-determining step shifts to the Heyrovsky step. The reduced Tafel slope and TOF demonstrate that light illumination promotes a faster Volmer–Heyrovsky reaction pathway. These findings demonstrate the improved HER kinetics and more efficient charge-transfer processes of NiCoP/g-C_3N_4 under photo-assisted conditions. Also, phosphorus incorporation improves electrical conductivity and modulates the electronic environment of the metal centres.[56] The presence of redox-active Ni and Co sites provides abundant active centres,[57] and these combined effects synergistically strengthen the intrinsic catalytic activity by promoting hydrogen adsorption, thereby accelerating the HER kinetics. Under illumination, additional photo-excited electrons (e^-) generated from g-C_3N_4 participate in the HER, enhancing the charge-transfer efficiency and lowering the Tafel slope. The observed Tafel slope of 85.9 mV dec^{-1} corresponds to the Volmer–Heyrovsky reaction pathway,[58] as illustrated in equations (eqn (3)–(6)). In contrast, under dark conditions, the absence of photogenerated carriers results in slower charge transfer and a higher overpotential, confirming the photo-assisted enhancement.

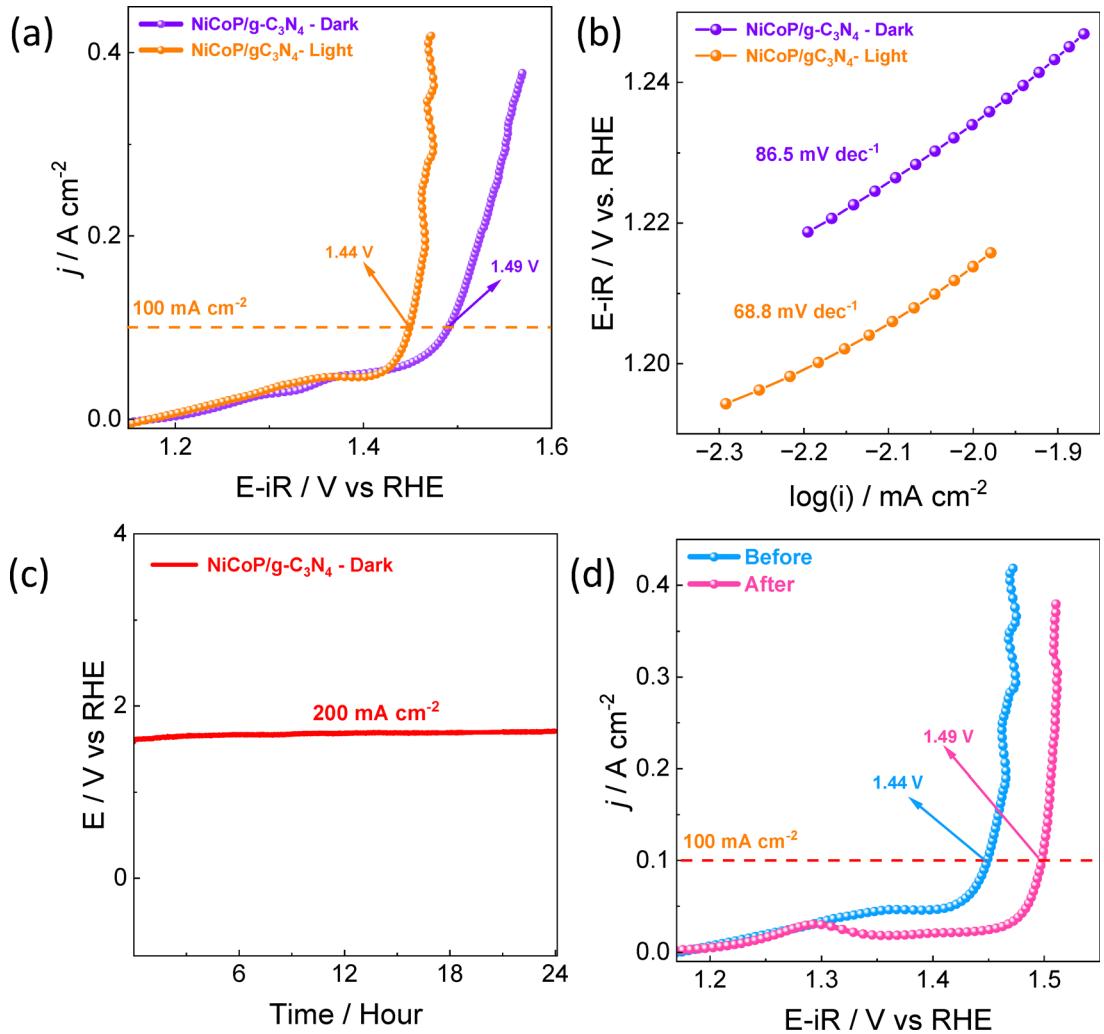

Fig. 10 (a) *iR* corrected LSV of NiCoP/g-C_3N_4 in dark and illuminated conditions, (b) Tafel plot of NiCoP/g-C_3N_4 in dark and illuminated conditions, (c) 24 hours of chronopotentiometry test for NiCoP/g-C_3N_4 under illuminated conditions at a current density of −200 mA cm^{-2}, and (d) *iR* corrected LSV of NiCoP/g-C_3N_4 in illuminated conditions before and after the chronopotentiometry test.

$$g\text{-}C_3N_4 + h\nu \rightarrow e^- + h^+ \quad \text{(photoexcitation of g-}C_3N_4\text{)} \quad (3)$$

$$M + H_2O + e^-_{photo} \rightarrow M\text{–}H_{ads} + OH^- \quad \text{(photo-assisted Volmer step)} \quad (4)$$

$$M\text{–}H_{ads} + H_2O + e^-_{photo} \rightarrow M + H_2 + OH^- \quad \text{(photo-assisted Heyrovsky step)} \quad (5)$$

$$M\text{–}H_{ads} + M\text{–}H_{ads} \rightarrow 2M + H_2 \quad \text{(Tafel step)} \quad (6)$$

To investigate the long-term electrochemical durability of the catalyst, chronopotentiometry was carried out at a high current density of -200 mA cm^{-2}. As shown in Fig. 9(c), the NiCoP/g-C_3N_4 catalyst demonstrated excellent long-term stability under illumination, maintaining a constant potential with negligible fluctuations over 24 h of continuous operation. In addition, LSV was conducted before and after the durability test, as shown in Fig. 9(d), and showed only a minor variation in overpotential (221 mV before and 209 mV after), confirming the structural and electrochemical robustness of the catalyst under prolonged high-current HER conditions. Long-term chronoamperometry was also performed for 12 hours, as shown in Fig. S3(b), the catalyst demonstrates stable performance without significant variations. These findings highlight the excellent stability and durability of the NiCoP/g-C_3N_4 catalyst.

The OER performance of the synthesised electrocatalysts is shown in Fig. 10(a), and the *iR*-corrected LSV polarisation curves demonstrate that the NiCoP/g-C_3N_4 catalyst exhibits significantly enhanced activity under illumination, requiring an overpotential of 210 mV to reach a current density of 100 mA cm^{-2}, whereas 260 mV is needed in the absence of light. Moreover, under illuminated conditions, the catalyst achieves a TOF of 3.18×10^{-5} s^{-1}, underscoring its excellent intrinsic catalytic activity. As presented in Fig. 10(b), the illuminated NiCoP/g-C_3N_4 catalyst delivers a Tafel slope of 68.8 mV dec^{-1}, which is markedly lower than the 86.5 mV dec^{-1} obtained in the dark. This reduction reflects improved OER kinetics and superior charge-transfer efficiency under photo-assisted conditions.

Under visible-light illumination, g-C_3N_4 generates electron–hole pairs, and the photogenerated electrons are transferred to NiCoP due to the Schottky contact at the NiCoP/g-C_3N_4 interface, enriching Ni/Co sites.[20,59] This illumination-induced electron accumulation dynamically tunes the Ni/Co d-orbital occupation and metal–oxygen covalency, thereby optimising the adsorption energies of *OH, *O and *OOH and facilitating their interconversion within the AEM pathway. Consequently, deprotonation of adsorbed water and the *OH → *O → *OOH steps proceed with lower energy barriers, promoting O–O bond formation and yielding the reduced Tafel slope and overpotential.[60] Furthermore, heteroatom coordination (P in NiCoP, N in g-C_3N_4) and interfacial Ni–N/Co–N bonds support efficient electron delocalisation between the active centres and adsorbed intermediates, so that illumination and interface-driven electron redistribution collectively account for the superior photo-assisted OER performance of NiCoP/g-C_3N_4.[44]

The long-term electrochemical stability of the NiCoP/g-C_3N_4 under illuminated conditions was further assessed through chronopotentiometric testing, as depicted in Fig. 10(c). The catalyst maintained a stable potential with negligible fluctuations over 24 hours, indicating excellent operational durability and stable operational performance. Post-stability LSV measurements, as shown in Fig. 10(d), revealed minimal shifts in the overpotential values before and after the stability assessment (210 mV and 260 mV at 100 mA cm^{-2}, respectively), and long-term chronoamperometry was also performed for 12 hours, as shown in Fig. S3(a), and the catalyst demonstrates stable performance without significant variations, further confirming the robust and sustained electrocatalytic performance of the NiCoP/g-C_3N_4 catalyst even under prolonged visible-light illumination. The LSV polarisation curves for the HER and OER of NiCo-MOF, NiCo/2.5%g-C_3N_4, NiCo/5%g-C_3N_4, NiCo/7.5%g-C_3N_4, and NiCoP are given in Fig. S2. The reproducibility of the

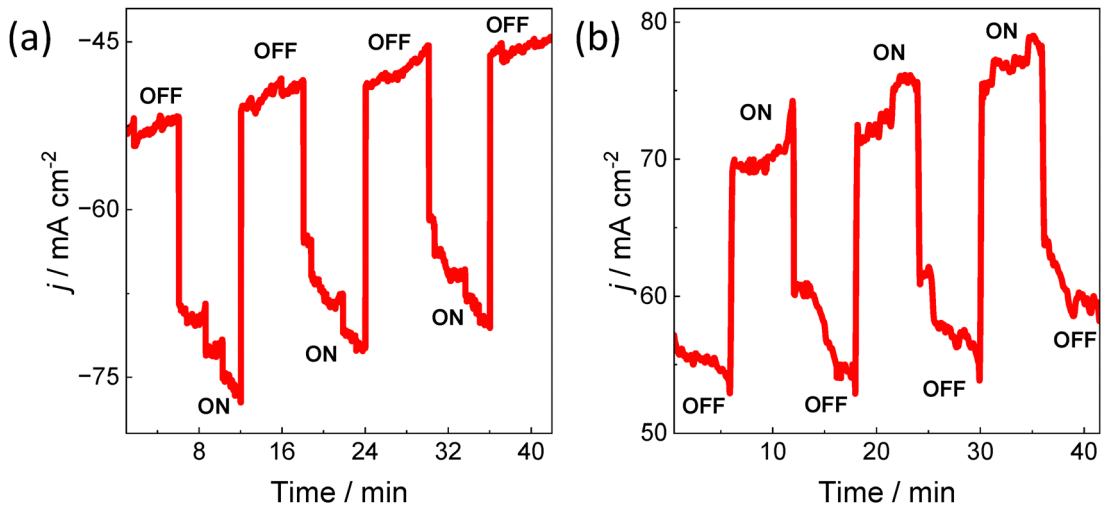

Fig. 11 Transient photocurrent response of the NiCoP/g-C_3N_4 electrode under chopped visible-light illumination recorded at (a) cathodic potential, and (b) anodic potential.

$NiCoP/g\text{-}C_3N_4$ catalyst under light illumination was validated using three separately fabricated electrodes for both the HER and OER, as shown in Fig. S5, indicating that the catalyst exhibits nearly identical performance.

To investigate the photoelectrochemical behaviour of the $NiCoP/g\text{-}C_3N_4$ electrode, chronoamperometric measurements were carried out under periodic visible-light illumination with ON–OFF cycles of 360 seconds. As depicted in Fig. 11(a), under cathodic potential, the electrode exhibited a pronounced increase in current density upon illumination, rising from -45.3 mA cm^{-2} in the dark to -77.3 mA cm^{-2} under light. The catalyst generates a current density 32 mA cm^{-2} higher than under dark conditions in the cathodic side, reflecting its strong sensitivity to visible light and efficient generation and separation of photogenerated charge carriers, thereby enhancing the HER process. Similarly, with anodic potential, as shown in Fig. 11(b), a significant increase in current density was observed, going from 52.8 mA cm^{-2} in the dark to 79 mA cm^{-2} under illumination. The catalyst exhibits an increase of 26.2 mA cm^{-2} under illumination compared to under dark conditions. This photo-assisted response demonstrates effective light utilisation and charge carrier separation by the catalyst, contributing to the enhanced OER performance.

The $NiCoP/g\text{-}C_3N_4$ catalyst, which demonstrated excellent HER and OER activities under illuminated conditions, was further evaluated for overall water-splitting performance in a two-electrode configuration using 1 M KOH, with the catalyst serving as both the anode and cathode. To examine stability, long-term chrono-potentiometric testing was performed at a high current density of 400 mA cm^{-2} for 24 hours under both dark and illuminated conditions, as shown in Fig. 12(a). The cell required markedly higher potential under dark conditions compared to illumination due to the absence of photogenerated carriers, which significantly hinders the catalytic activity. Under illumination, the heterojunction reduced the energy barrier, which in turn lowered the operating potential, thereby proving the beneficial role of photo-assistance in overall water splitting. The cell voltage remained stable throughout the test, confirming the exceptional durability of the catalyst. As shown in Fig. 12(b), the LSV polarisation curves reveal that the cell required 1.65 V under dark conditions to achieve a current density of 10 mA cm^{-2}, whereas under illumination the

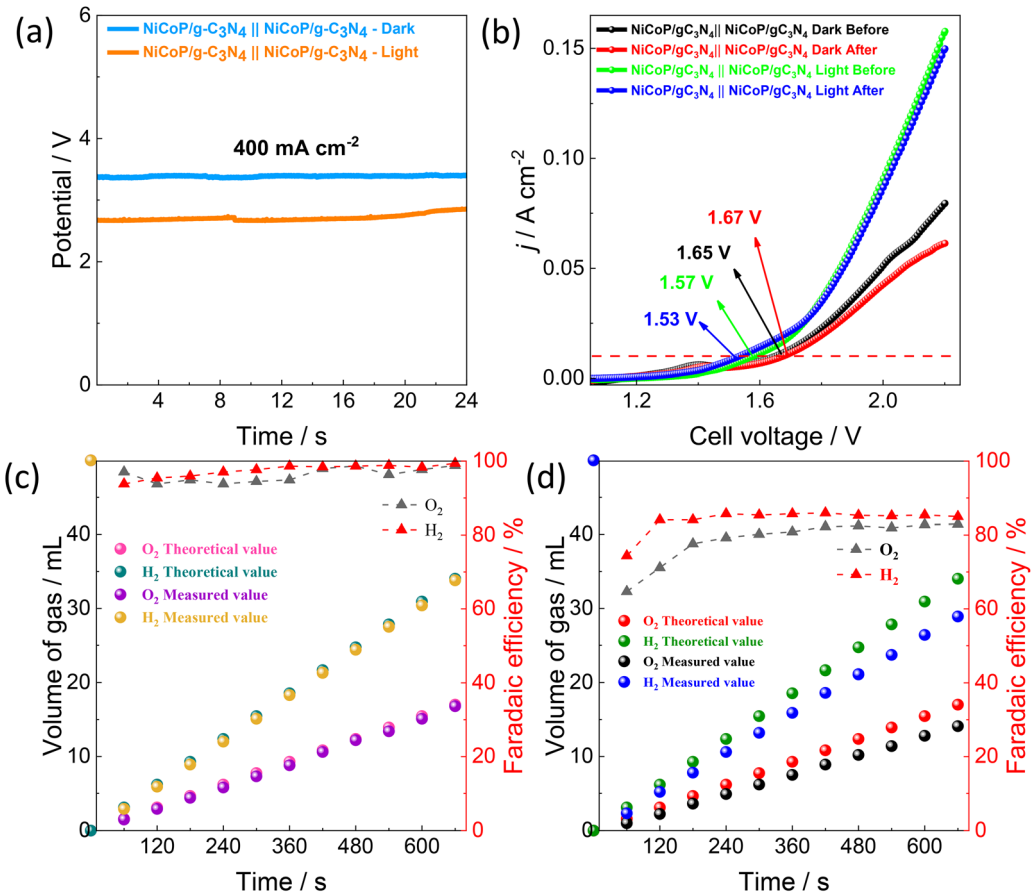

Fig. 12 (a) 24 hours of chrono potentiometric test of $NiCoP/g\text{-}C_3N_4 \| NiCoP/g\text{-}C_3N_4$ at a current density of 400 mA cm^{-2}, (b) LSV of $NiCoP/g\text{-}C_3N_4 \| NiCoP/g\text{-}C_3N_4$ before and after the chrono potentiometric test in dark and illuminated conditions, (c) and (d) plots of the volumes of H_2 and O_2 released for $NiCoP/g\text{-}C_3N_4 \| NiCoP/g\text{-}C_3N_4$ at a current density of 400 mA cm^{-2} and its faradaic efficiency under illuminated and dark conditions, respectively.

Table 1 Performance comparison of NiCoP/g-C_3N_4 in dark and light conditions with recently reported MOF and g-C_3N_4-based electrocatalysts for water splitting

MOF electrode	η (mV@mA cm^{-2})		Tafel slope (mV dec^{-1})		Overall water splitting (V@mA cm^{-2})	Ref.
	HER	OER	HER	OER		
$NiCo_2S_4$@S-g-C_3N_4	415/10	370/10	230	99.2	—	61
CoFe-LDH@g-C_3N_4	417/10	275/10	77	51	1.55@10	62
3 wt% g-C_3N_4@ZIF67	176/10	152/10	165	90	1.34@10	16
Fe-MOF@MoS_2-6h	118/10	187/10	68	61	1.51@10	4
NiFe-MOF-5	163/10	168/10	139	42	1.57@10	63
$NiCo_{(nf)}$–P	199/100	315/100	112	66	1.74@100	64
NiCoFeP/C	149/10	270/10	108	65	1.60/10	65
NiCo-LDH@NH_2-UiO-66	224@50	296@50	82	56	1.65@10	66
NiCoP/g-C_3N_4 (dark)	277@100	260@100	98	86	1.65@10	This work
NiCoP/g-C_3N_4 (light)	222@100	210@100	85	68	1.53@10	This work

required voltage decreased significantly to 1.57 V, underscoring the beneficial impact of the photo-assisted system in enhancing overall water splitting. Furthermore, LSV measurements conducted after the long-term stability test revealed a negligible difference in cell potential (Fig. 12(b)), highlighting the robustness of the catalyst under prolonged operation. Under illuminated conditions, the NiCoP/g-C_3N_4 catalyst exhibits a mass activity of 7.69 A g^{-1} at an applied potential of 2.03 V. The catalyst exhibits high intrinsic activity, achieving an ECSA-normalized current density of 100 mA cm$^{-2}{}_{ECSA}$ at 1.57 V, indicating the efficient utilisation of electrochemically active sites. The post-stability morphology of the electrodes, together with the corresponding EDS spectra, is presented in Fig. S7, confirming the structural and compositional stability of the catalyst after long-term operation. These results validate NiCoP/g-C_3N_4 as a highly stable and efficient bifunctional electrode under visible-light illumination, demonstrating significant potential for practical overall water-splitting applications.

The amounts of hydrogen (H_2) and oxygen (O_2) generated in the two-electrode NiCoP/g-C_3N_4 system were measured using an inverted burette setup. Fig. 12(c) presents the theoretical and experimental volumes of H_2 and O_2 gases evolved during the operation of the NiCoP/g-C_3N_4 electrode under illuminated conditions at a current density of 400 mA cm^{-2}. Gas volumes were subsequently recorded at 60-second intervals. Prior to the experiment, the 1 M KOH was purged with nitrogen gas for 15 minutes to remove dissolved oxygen. The theoretical values were calculated based on Faraday's law of electrolysis in combination with the ideal gas law (eqn (S4)). The average Faradaic efficiencies were determined to be 97.46% for HER and 96.22% for OER. The associated burette reading measurement error was estimated to be $\pm$0.2 mL. The corresponding gas evolution profiles recorded under dark conditions are shown in Fig. 12(d), and the average Faradaic efficiencies were determined to be 78.76% for the OER and 84.17% for the HER. A digital image of the inverted burette setup used to measure the evolved H_2 and O_2 gases is shown in Fig. S6. The performance comparison of NiCoP/g-C_3N_4 under dark and light conditions is presented alongside recently reported MOF and g-C_3N_4-based electrocatalysts for water splitting, as summarised in Table 1.

The approximate energy required by the NiCoP/g-C_3N_4 electrode under illuminated conditions to generate 1 kg of H_2 and O_2 in 1 M KOH was calculated using eqn (S6). The total charge (Q) necessary for hydrogen generation in the two-electrode system was determined to be 98 201 093.49 C, while that required for oxygen was 6 266 397.32 C. Based on eqn (S6), the corresponding electrical energy was calculated using a cell voltage (U) of 2.03 V at a current density of 100 mA cm^{-2} in 1 M KOH. The resulting energy demands for hydrogen and oxygen evolution were 199 348 219.8 J (55.37 kWh) and 12 720 786.5 J (3.53 kWh), respectively. These findings demonstrate that the NiCoP/g-C_3N_4 electrode achieves efficient overall water splitting under illumination, with relatively low energy consumption for both hydrogen (H_2) and oxygen (O_2) generation.

4. Conclusion

In conclusion, the NiCoP/g-C_3N_4 heterostructure, synthesised *via in situ* growth of NiCo-MOF on an optimised amount of g-C_3N_4 followed by phosphidation, has shown exceptional bifunctional electrocatalytic activity for overall water splitting. Under visible-light irradiation, the NiCoP/g-C_3N_4 heterostructure exhibited enhanced performance, with low overpotentials of 222 mV for the HER and 210 mV for the OER at a current density of 100 mA cm^{-2}, representing a decrease in overpotential by 1.25-fold compared to dark conditions. This enhanced activity is attributed to the synergistic interaction of g-C_3N_4 and NiCoP, which enables efficient light absorption, rapid charge separation, and directional electron transport across the heterointerface. The catalyst also demonstrated excellent stability in a two-electrode configuration, for 24 hours at a high current density of 400 mA cm^{-2}, with Faradaic efficiencies of 97% for the HER and 96% for the OER. These findings underscore the significance of light-assisted electrochemical water splitting in enhancing charge-transfer processes and establishing a cost-effective, non-noble-metal heterostructure for efficient and sustainable hydrogen production.

Conflicts of interest

There are no conflicts to declare.

Data availability

All data supporting the findings of this study are available within the article and the accompanying supplementary information (SI). Supplementary information: material characterisation data, additional electrochemical studies, EIS circuit parameter table, EDS image and reproducibility data. See DOI: https://doi.org/10.1039/d5ma01279a.

Acknowledgements

The author (MPN) would like to thank NITK for the Research Fellowship support and the Central Research Facility (CRF) for providing access to their vast facilities for characterisation.

References

1 M. G. Rasul, M. A. Hazrat, M. A. Sattar, M. I. Jahirul and M. J. Shearer, *Energy Convers. Manage.*, 2022, **272**, 116326.
2 F. Chen, L. Bao, Y. Zhang, R. Wang, J. Liu, W. Hai and Y. Liu, *Sensors*, 2023, **23**, 4348.
3 Z. Wang, S. Li, G. Zhang, X. Yu, Z. Zhao, Y. Zhang, Y. Shi, H.-B. Zhu and X. Xiao, *Appl. Catal., B*, 2024, **342**, 123387.
4 R. Velayutham, C. J. Raj, H. M. Jang, W.-J. Cho, K. Palanisamy, C. Kaya and B. C. Kim, *Mater. Today Nano*, 2023, **24**, 100387.
5 B. Zhang, Y. Zheng, T. Ma, C. Yang, Y. Peng, Z. Zhou, M. Zhou, S. Li, Y. Wang and C. Cheng, *Adv. Mater.*, 2021, **33**, 2006042.
6 W. Zheng and L. Y. S. Lee, *ACS Energy Lett.*, 2021, **6**, 2838–2843.
7 T. Shaikh, S. Pise, R. Bhosale, M. Vadiyar, K.-W. Nam and S. Kolekar, *Energy Fuels*, 2025, **39**, 2396–2421.
8 H. Li, L. Li, R.-B. Lin, W. Zhou, Z. Zhang, S. Xiang and B. Chen, *EnergyChem*, 2019, **1**, 100006.
9 T. Qiu, Z. Liang, W. Guo, H. Tabassum, S. Gao and R. Zou, *ACS Energy Lett.*, 2020, **5**, 520–532.
10 B. Singh and H. Gupta, *Chem. Commun.*, 2024, **60**, 8020–8038.
11 X. Ma, K. Qi, S. Wei, L. Zhang and X. Cui, *J. Alloys Compd.*, 2019, **770**, 236–242.
12 H. Hayat, T. Noor, N. Iqbal, R. Ahmed, N. Zaman and Y. Huang, *J. Environ. Chem. Eng.*, 2023, **11**, 109627.
13 E. S. Sowbakkiyavathi, P. Dhandapani, S. Ramasamy, J. H. Oh, I. In, S. J. Lee and A. Subramania, *RSC Sustainability*, 2025, **3**, 3628–3651.
14 M. Ubaidullah, A. M. Al-Enizi, S. Shaikh, M. A. Ghanem and R. S. Mane, *J. King Saud Univ., Sci.*, 2020, **32**, 2397–2405.
15 B. Shabbir, K. Jabbour, S. Manzoor, M. F. Ashiq, K. F. Fawy and M. N. Ashiq, *Heliyon*, 2023, **9**, e20261.
16 S. Khan, T. Noor, N. Iqbal, E. Pervaiz and L. Yaqoob, *RSC Adv.*, 2023, **13**, 24973–24987.
17 B. Gibbons, D. R. Cairnie, B. Thomas, X. Yang, S. Ilic and A. J. Morris, *Chem. Sci.*, 2023, **14**, 4672–4680.
18 L. Rao, J. D. Rodney, A. Joy, C. Shivangi Nileshbhai, A. James, S. S. F. Joyline Mascarenhas, N. K. Udayashankar, P. Anjukandi, B. Chul Kim and B. Ramachandra Bhat, *Chem. Eng. J.*, 2024, **500**, 156639.
19 Z. Sun, Y. Li, S. Zhang, L. Shi, H. Wu, H. Bu and S. Ding, *J. Mater. Chem. A*, 2019, **7**, 11069–11076.
20 S. Cao and J. Yu, *J. Phys. Chem. Lett.*, 2014, **5**, 2101–2107.
21 X. Liu, P. Wang, H. Zhai, Q. Zhang, B. Huang, Z. Wang, Y. Liu, Y. Dai, X. Qin and X. Zhang, *Appl. Catal., B*, 2018, **232**, 521–530.
22 Y. Liu, H. Zhang, J. Ke, J. Zhang, W. Tian, X. Xu, X. Duan, H. Sun, M. O. Tade and S. Wang, *Appl. Catal., B*, 2018, **228**, 64–74.
23 S. Chen, J. Wei, X. Ren, K. Song, J. Sun, F. Bai and S. Tian, *Molecules*, 2023, **28**, 4283.
24 P. H. Linh, P. Do Chung, N. Van Khien, L. T. M. Oanh, V. T. Thu, T. N. Bach, L. T. Hang, N. M. Hung and V. D. Lam, *Diamond Relat. Mater.*, 2021, **111**, 108214.
25 T. Tian, L. Ai and J. Jiang, *RSC Adv.*, 2015, **5**, 10290–10295.
26 X. Zhang, C. Jia, Y. Xue and P. Yang, *RSC Adv.*, 2017, **7**, 43888–43893.
27 X. Xia, B. Xu, H. Zhang, K. Ji, X. Ji, D. Wang and P. Yang, *J. Alloys Compd.*, 2022, **928**, 167207.
28 J. Li, H. Wang, Z. Guo, Y. Wang, H. Ma, X. Ren, B. Du and Q. Wei, *Talanta*, 2017, **162**, 46–51.
29 T. Song, C. Xie, K. Matras-Postolek and P. Yang, *J. Phys. Chem. C*, 2021, **125**, 19382–19393.
30 R. Bernasconi, M. I. Khalil, C. Iaquinta, C. Lenardi, L. Nobili and L. Magagnin, *ACS Appl. Energy Mater.*, 2020, **3**, 6525–6535.
31 Z. Lv, M. Wang, D. Liu, K. Jian, R. Zhang and J. Dang, *Inorg. Chem.*, 2021, **60**, 1604–1611.
32 B. Zhang, S. Xu, J. Li, X.-X. Zhao, R. Zhao, M. Zhang, D. Zhao and L. Miao, *CrystEngComm*, 2025, **27**, 5485–5500.
33 A. P. Grosvenor, M. C. Biesinger, R. S. C. Smart and N. S. McIntyre, *Surf. Sci.*, 2006, **600**, 1771–1779.
34 Y. Lu, Y. Deng, S. Lu, Y. Liu, J. Lang, X. Cao and H. Gu, *Nanoscale*, 2019, **11**, 21259–21265.
35 C. Jin, C. Xu, W. Chang, X. Ma, X. Hu, E. Liu and J. Fan, *J. Alloys Compd.*, 2019, **803**, 205–215.
36 J. Shi, F. Qiu, W. Yuan, M. Guo and Z.-H. Lu, *Chem. Eng. J.*, 2021, **403**, 126312.
37 G. Arunkumar, P. Muthukumar, G. Deviga, M. Mariappan, M. Pannipara, A. G. Al-Sehemi and S. P. Anthony, *New J. Chem.*, 2024, **48**, 1671–1677.
38 F. Wei, Y. Liu, H. Zhao, X. Ren, J. Liu, T. Hasan, L. Chen, Y. Li and B.-L. Su, *Nanoscale*, 2018, **10**, 4515–4522.
39 M. Ramstedt and A. Shchukarev, *Surf. Sci. Spectra*, 2024, **31**, 024016.
40 Y. Zhang, Y. Liu, M. Ma, X. Ren, Z. Liu, G. Du, A. M. Asiri and X. Sun, *Chem. Commun.*, 2017, **53**, 11048–11051.
41 J. Wu, X. Ge, Z. Li, D. Cao and J. Xiao, *Electrochim. Acta*, 2017, **252**, 101–108.
42 K. Tao, Y. Gong and J. Lin, *Nano Energy*, 2019, **55**, 65–81.
43 C. Zhang, Z. Pu, I. S. Amiinu, Y. Zhao, J. Zhu, Y. Tang and S. Mu, *Nanoscale*, 2018, **10**, 2902–2907.
44 C. Li, H. Wu, Y. Du, S. Xi, H. Dong, S. Wang and Y. Wang, *ACS Sustainable Chem. Eng.*, 2020, **8**, 12934–12943.

45 M. Fiaz, N. Carl, M. Kashif, M. A. Farid, N. N. Riaz and M. Athar, *RSC Adv.*, 2022, **12**, 32110–32118.
46 H. Ma, J. Feng, F. Jin, M. Wei, C. Liu and Y. Ma, *Nanoscale*, 2018, **10**, 15624–15631.
47 G. Z. S. Ling, V. B.-Y. Oh, C. Y. Haw, L.-L. Tan and W.-J. Ong, *Energy Mater. Adv.*, 2023, **4**, 0038.
48 S. Anantharaj, S. R. Ede, K. Karthick, S. Sam Sankar, K. Sangeetha, P. E. Karthik and S. Kundu, *Energy Environ. Sci.*, 2018, **11**, 744–771.
49 F.-Y. Liang, H.-W. Huang, Y.-C. Chen and P.-J. Huang, *Energy Fuels*, 2025, **39**, 6533–6548.
50 A. Tarighati Sareshkeh, M. S. Seyed Dorraji, Z. Karami, S. Shahmoradi, E. Fekri, H. Daneshvar, M. H. Rasoulifard and D. N. Karimov, *Sci. Rep.*, 2023, **13**, 15079.
51 S. Jung, C. C. L. McCrory, I. M. Ferrer, J. C. Peters and T. F. Jaramillo, *J. Mater. Chem. A*, 2016, **4**, 3068–3076.
52 R. S. Nicholson and I. Shain, *Anal. Chem.*, 1965, **37**, 190–195.
53 L. Rao, J. D. Rodney, Shivakumar, U. K. Dalimba, N. K. Udayashankar, B. C. Kim and B. R. Bhat, *Microchem. J.*, 2024, **204**, 111172.
54 A. Jamma, B. Jaksani, C. S. Vennapoosa, S. Gonuguntla, S. Sk, M. Ahmadipour, M. Abraham B., I. Mondal and U. Pal, *Mater. Adv.*, 2024, **5**, 2785–2796.
55 K. Hidayatullah, J. Manopo, I. Supu, A. Hadju, C. Ofiyen, M. K. Mahardhika and Y. Darma, *Inorg. Chem. Commun.*, 2025, **179**, 114885.
56 X. Tang, N. Li and H. Pang, *Green Energy Environ.*, 2022, **7**, 636–661.
57 B. Cui, C. Wang, S. Huang, L. He, S. Zhang, Z. Zhang and M. Du, *J. Colloid Interface Sci.*, 2020, **578**, 10–23.
58 S. Shin, Z. Jin, D. H. Kwon, R. Bose and Y.-S. Min, *Langmuir*, 2015, **31**, 1196–1202.
59 M. G. Sahini, A. Parmain, I. Onoka and S. F. Mwanga, *J. Alloys Compd.*, 2025, **1044**, 183642.
60 B. Wang, T. Fukushima, H. Minamimoto, A. Lyalin, K. Murakoshi and T. Taketsugu, *Commun. Chem.*, 2025, **8**, 109.
61 H. D. Khalid, A. Bilal, M. Javed, A. Amjad, A. Ali, A. Bahadur, S. Iqbal, S. Mahmood, T. A. Saleh, A. Rana, N. S. Awwad and H. A. Ibrahium, *Int. J. Hydrogen Energy*, 2024, **68**, 128–138.
62 M. Arif, G. Yasin, M. Shakeel, M. A. Mushtaq, W. Ye, X. Fang, S. Ji and D. Yan, *Mater. Chem. Front.*, 2019, **3**, 520–531.
63 Q. Mou, Z. Xu, G. Wang, E. Li, J. Liu, P. Zhao, X. Liu, H. Li and G. Cheng, *Inorg. Chem. Front.*, 2021, **8**, 2889–2899.
64 Z. Xu, C.-L. Yeh, J.-L. Chen, J. T. Lin, K.-C. Ho and R. Y.-Y. Lin, *ACS Sustainable Chem. Eng.*, 2022, **10**, 11577–11586.
65 X. Wei, Y. Zhang, H. He, L. Peng, S. Xiao, S. Yao and P. Xiao, *Chem. Commun.*, 2019, **55**, 10896–10899.
66 S. Sk, R. Madhu, D. S. Gavali, V. Bhasin, R. Thapa, S. N. Jha, D. Bhattacharyya, S. Kundu and U. Pal, *J. Mater. Chem. A*, 2023, **11**, 10309–10318.